Active Complexes on Engineered Crystal Facets of MnO_x–CeO_2 and Scale-up Demonstration on an Air Cleaner for Indoor Formaldehyde Removal

Haiwei Li,[†] Wingkei Ho,[‡,§] Junji Cao,[ǁ] Duckshin Park,[ǁǁ] Shun-cheng Lee,*[,†] Yu Huang *[,ǁ]

[†]Department of Civil and Environmental Engineering, The Hong Kong Polytechnic University, Hong Kong, China.

[‡]Department of Science and Environmental Studies, The Education University of Hong Kong, Hong Kong, China.

[§]State Key Laboratory of Marine Pollution, The City University of Hong Kong, Hong Kong, China.

[ǁ]State Key Laboratory of Loess and Quaternary Geology (SKLLQG) and Key Laboratory of Aerosol Chemistry and Physics, Institute of Earth Environment, Chinese Academy of Sciences, Xi'an 710061, China.

[ǁǁ]Transportation Environmental Research Team, The Korea Railroad Research Institute, Gyeonggi-do, South Korea.

Corresponding Authors: Prof. Shuncheng Lee, E-mail: ceslee@polyu.edu.hk; Prof. Yu Huang, E-mail: huangyu@ieecas.cn.

21

TOC Art

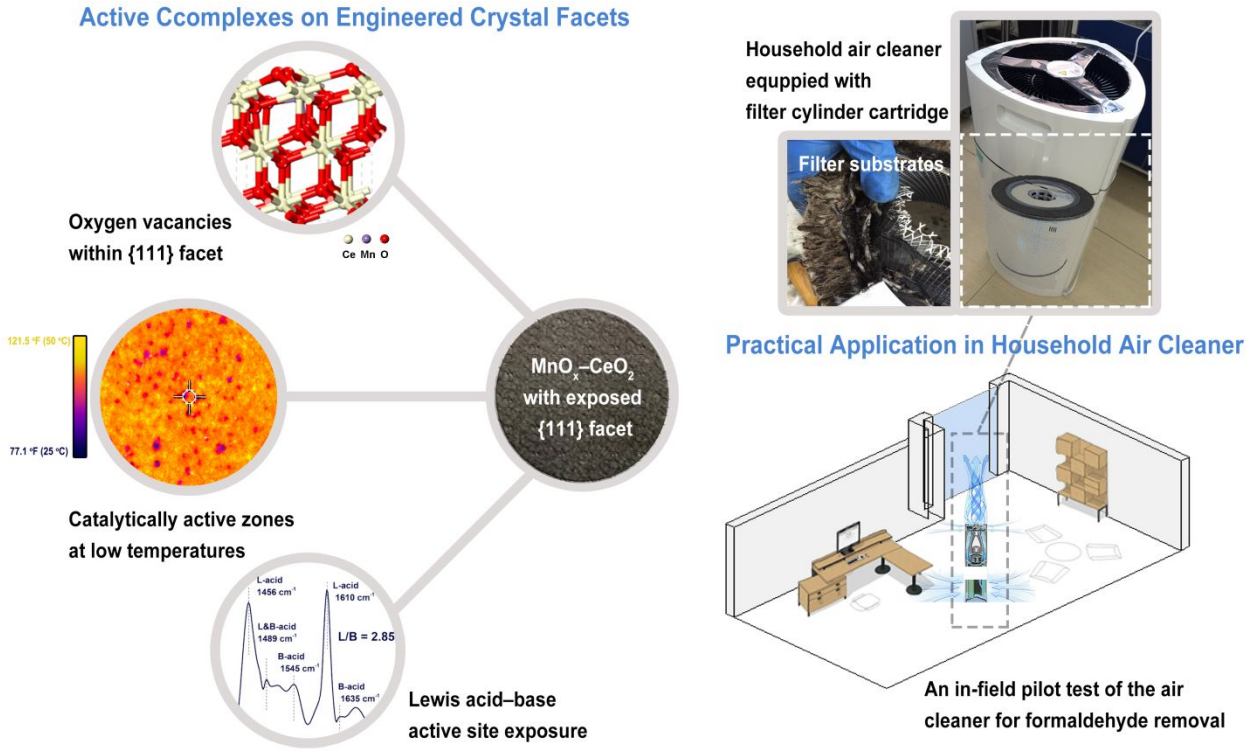

22
23

ABSTRACT: Crystal facet-dominated surfaces determine the formation of surface-active complexes, and engineering specific facets is desirable for improving the catalytic activity of routine transition metal oxides that often deactivate at low temperatures. Herein, MnO_x–CeO_2 was synthetically administered to tailor the exposure of three major facets, and their distinct surface-active complexes concerning the formation and quantitative effects of oxygen vacancies, catalytically active zones, and active-site behaviors were unraveled. Compared with two other low-index facets {110} and {001}, MnO_x–CeO_2 with exposed {111} facet showed higher activity for formaldehyde oxidation and CO_2 selectivity. However, the {110} facet did not increase activity despite generating additional oxygen vacancies. Oxygen vacancies were highly stable on the {111} facet and its bulk lattice oxygen at rapid migration rates could replenish the consumption of surface lattice oxygen, which was associated with activity and stability. High catalytically active regions were exposed at the {111}-dominated surfaces, wherein the predominated Lewis acid–base properties facilitated oxygen mobility and activation. The mineralization pathways of formaldehyde were examined by a combination of *in situ* X-ray photoemission spectroscopy and diffuse reflectance infrared Fourier transform spectrometry. The MnO_x–CeO_2-111 catalysts were subsequently scaled up to work as filter substrates in a household air cleaner. In an in-field pilot test, 8 h of exposure to an average concentration of formaldehyde after start-up of the air cleaner attained the Excellent Class of Indoor Air Quality Objectives in Hong Kong.

INTRODUCTION

MnO_x–CeO_2 mixed oxides have been examined in the catalytic oxidation of priority gaseous pollutants, such as formaldehyde (HCHO)[1-4], carbon monoxide (CO)[5], and nitrogen oxides (NO_x)[6, 7]. Given reactive metal–particle interfaces, the promoting effect of noble metal nanoparticles on MnO_x–CeO_2 mixed oxides (e.g., Ag/MnO_x–CeO_2[8] and Pt/MnO_x–CeO_2[9]) has been obtained during the nearly complete oxidation of HCHO at low temperatures. To date, the industrial development of relatively inexpensive but effective noble metal-free catalysts is needed, and catalyst deactivation occurs at ambient temperature[1, 10].

Surface-active complexes concerning defect formation, activation of reactive oxygen species, molecule adsorption, and heterogeneous oxidation are proportional to exposed crystal facets. Engineering crystal facets induces distinct oxygen vacancy clusters within different exposed facets and possess various physical and chemical performances of structured crystal atoms[11, 12]. From an industrial perspective, engineering surface structures for binary transition metal oxides is more apt to their scale-up production relative than either single nanostructured oxidized metals or ternary junctions[13-15], because the reactivity and facet control are often uncertain in the Mars–Van Krevelen redox mechanisms of heterogeneous catalysis[1, 13] or in a solid solution containing complex solvents or additives[2, 11]. As such, ceria with a fluorite structure has three major low-index facets: nanocubes preferentially dominated by the {110} facet and nanorods dominated by the {111} and {100} facets[16, 17]. The exposed {110} and {100} facets can facilitate the migration of lattice oxygen from the bulk to the surface, but the process is restricted on the {111} surfaces[18]. However, the dominant {110} and {100} facets are inclined to deactivate with reaction time because of the low stability of the oxygen vacancies employed[16-19]. The stability of CeO_2 nanocrystals can be maintained by doping with stable metals, such as

Mn, Ti, or Zr[2, 18, 20, 21]. By contrast, when manganese ions (Mn^{n+}) with small ionic radius and low composition are stabilized in MnO_x–CeO_2 mixed oxides, the oxygen mobility is strongly affected, and higher catalytic activities are achieved at low temperatures than single oxidized metals[1-3, 9, 15]. In MnO_x–CeO_2 mixed oxides, ceria is not directly involved in catalytic oxidation but functions as an oxygen carrier to keep high-valence manganese oxide via a Mn dismutation reaction. Moreover, the enhancement of reactivity is ascribed to the mobility and activation of lattice oxygen[17, 22]. Exposing specific crystal facets remains challenges. The exposed facets with high surface energy can decline with a fast growth rate in the bulk of crystals; hence, the thermodynamically stable facets predominated on crystal surfaces could minimize the total surface energy[11]. Key factors, such as solvents, additives, and impurities in a solid solution, can also influence the final shape of crystals. Therefore, appropriate surfactant-assisted/capping agents (e.g., citric acid and cetyltrimethylammonium bromide) have been chosen to tailor the exposure of crystal facets[1, 2, 11, 17]. For example, the ceria {001} facet with fast growth was well administered using decanoic acid as an organic ligand molecules[23]. Aside from the facet reforming and growth, a large amplitude of catalytically active regions is indispensable for exposed surface-active complexes within facet-dominated surfaces[24, 25].

Translating laboratory work into commercial value at large is the focus of our research. The situation of indoor air pollution is aggravated by numerous factors, including high-rise living, subdivided flats, and lack of windows and ventilation in most enclosed areas. Considering the toxicity of HCHO at very low concentrations, standards for the emission levels of HCHO have become stringent in the Indoor Air Quality Certification Scheme in Hong Kong, i.e., Excellent Class with 30 $\mu g \cdot m^{-3}$ and Good Class with 100 $\mu g \cdot m^{-3}$ for an 8 h of exposure[26, 27]. To eliminate HCHO in indoor air, our group developed various collosol-film coating, purifier filter substrates,

or honeycomb-like reactors based on heterogeneous catalysis to use in different environments[28, 29]. Knowledge gained from laboratory tests and field campaigns can be used to estimate the best-case scenario for the formulation and development of mitigation strategies.

Herein, MnO_x–CeO_2 catalysts with different major exposed facets were synthesized using varying morphology-controlling methods. The exposed three major {111}, {110}, and {001} facet-dominated surfaces were systematically studied in terms of activity and selectivity, formation and quantitative effects of oxygen vacancies, identification of catalytically active regions, and intermediate pathways. Efficient MnO_x–CeO_2-111 catalysts were scaled up to function as filter substrates of a household air cleaner. The materials obtained from the laboratory-scale experiments were examined and validated in an in-field pilot test of the air cleaner to evaluate their actual removal effectiveness.

MATERIALS AND METHODS

Catalyst Synthesis. MnO_x–CeO_2-111 (denoted as MCO-111) was synthesized by a hydrothermal redox reaction containing $Mn(NO_3)_2$ (50 vol%, 8 mM), $Ce(NO_3)_3 \cdot 6H_2O$ (8 mM), and $(NH_4)_2S_2O_8$ (16 mM). The resulting mixture was transferred into a 50 mL Teflon-lined stainless-steel autoclave after stirring for 2 h and then heated at 140 °C for 12 h. The hydrothermal products were washed with ultrapure water (Milli-Q system, Millipore Inc.), dried at 70 °C, and calcined at 350 °C for 6 h. Finally, the calcined products were treated with 100 mL of citric acid solution (2 mM) before washing and drying.

MnO_x–CeO_2-110 (MCO-110) was prepared by co-precipitation. A mixture of the same $Mn(NO_3)_2$ (50 vol%, 8 mM) and $NH_4Ce(NO_3)_4 \cdot 6H_2O$ (8 mM) solution was dissolved in ultrapure water followed by the dropwise addition of the precipitant NaOH solution (20 mM). The resulting solution was added to an aqueous solution of cetyltrimethylammonium bromide

(CTAB, Sigma ≥ 98%) under stirring for 2 h and then heated at 70 °C for 12 h. The harvested gel precipitates were washed and filtered before drying at 70 °C and calcining at 500 °C for 6 h.

MnO_x–CeO_2-001 (MCO-110) was prepared with the synthesis route similar to that of MCO-111 but the mixture was added with organic ligand molecules, i.e., decanoic acid (50 mg). After the hydrothermal reaction at 400 °C for 1 h and quenching in a water bath to room temperature, the organic ligand-modified products were extracted from a mixture of 3 mL of hexane and 15 mL of ethanol. Considering that the precursor CeO_2 {001} surface is less stable than the {111} surface, the organic ligand molecules can lead to the formation of the exposed {001} surface toward the crystal growth in the [111] direction instead of the [001] direction[23].

Characterizations. The as-prepared catalysts were characterized by the following techniques: X-ray powder diffraction (XRD; Philips X'pert Pro Super diffractometer), high-resolution transmission electron microscopy (HRTEM; JEOL JEM-2010), Brunauer–Emmett–Teller analysis (BET; Micromeritics Gemini VII 2390 Norcross, GA), thermogravimetric analysis (TGA; Setaram Setsys 16/18 thermoanalyzer), inductively coupled plasma atomic emission spectroscopy (ICP-AES; Varian), H_2 temperature-programmed reduction (H_2–TPR), O_2 temperature-programmed desorption (O_2–TPD), X-ray photoemission spectroscopy (XPS; Thermo ESCALAB 250Xi) calibrated with C 1s at 284.8 eV, and pyridine adsorbed IR spectroscopy (Py-IR; Tensor 27, Bruker). Some detailed methods are proved in **Supporting Information (SI),** and infrared thermography (IRT; FLIR camera SC7000 system) is illustrated in **SI Figures S1–S2 and Table S1**.

Laboratory Activity Test. Under the reaction condition of 5 ppm HCHO/21 vol% O_2/N_2 and gas hourly space velocity (GHSV) = 4×10^4 h^{-1}, the catalytic activity for the conversion of HCHO into CO_2 was tested in a thermostatic fixed-bed reaction system, as described in **SI**.

Designed H_2–TPR Experiments. The quantitative effects of oxygen vacancies within different exposed facets were evaluated through the consumption of reductant H_2 with lattice oxygen in two types of designed H_2–TPR experiments, i.e., the migration of bulk lattice oxygen (O) treated at 600 °C and the consumption of surface lattice oxygen treated at 450 °C, wherein the two types of lattice oxygen of MCO catalysts were ran into release and decline, also obtained from the TGA profile (**SI Figure S3**). The samples were pretreated similarly to the H_2–TPR measurements (see in **SI**) and heated to 600 °C at a heating rate of 10 °C·min^{-1} for various treatment periods (1, 5, and 10 h) under 10 vol% H_2/Ar gas flow. The corresponding H_2 consumption was monitored by using an online thermal conductivity detector to calculate the migration amount of bulk lattice oxygen after reheating to 950 °C. The pretreated samples in the second experiment were treated at 450 °C under identical treatment conditions and then cooled to 100 °C under ultra-pure Ar feed. After reheating to 950 °C, the corresponding H_2 consumption was recorded in a similar manner to calculate the consumption amount of surface lattice oxygen.

***In Situ* XPS and Diffuse Reflectance Infrared Fourier Transform Spectrometry (DRIFT) Analysis.** The detailed *in situ* XPS and DRIFT experiments are described in **SI**. The assignment of C 1s XPS photopeaks is listed in **SI Table S2** in accordance with the binding energies (BEs) of different possible chemical bonds.

RESULTS AND DISCUSSION

Structural Characterizations. The characteristic peaks of MCO with different exposed facets shifted toward low 2θ angles, as shown in **Figure 1a**. This low-angle shift was ascribed to the facet growth after some Ce^{4+} ions (0.087 nm) of ceria were replaced with Mn^{n+} of a small ionic radius (i. e., Mn^{4+} of 0.053 nm and Mn^{3+} of 0.065 nm) in the mixed oxides[4]. The crystal structures (**SI Table S3**) and redox properties of MCO catalysts were enhanced relative to bare

158 MnO_x and CeO_2 when the molar ratio of Mn/(Mn+Ce) was administered below 0.5 in the mixed
159 oxides[2, 4, 9]. High Mn content can enlarge the surface area but is often mobilized after rigorous
160 aging treatment[15]. In comparison with the MCO-110 and MCO-100 facets, a faint characteristic
161 peak related to manganese dioxide (2θ of (101) = 28.7°, JCPDS No. 24-735) was observed for
162 MCO-111, because the Mn_3O_4 phases (an ionic structure of $Mn^{2+}(Mn^{3+})_2O_4$, JCPDS No. 071841)
163 were restricted in the presence of the stable lattice plane {111} of the precursor ceria after acid
164 treatment[2]. Relative to the pristine {111} facet dominated in ceria nanoparticles and the pristine
165 {110} facet in ceria nanorods (see **SI Figure S4**), Mn^{n+} doping could reform the surfaces: the
166 MCO-111 and MCO-110 surfaces became cylindrical, and their corresponding framework
167 architectures changed from facetted pores and channels to smooth pores and channels within the
168 well-defined {111} and {100}-dominated surfaces (**Figure 1b**). The crystallite size of the
169 different MCO samples remained unchanged if Mn content in the mixed oxides was approaching
170 (**SI Table S3**). Both MCO-111 and MCO-110 demonstrated similar crystallite size with a
171 diameter of approximately 50 nm in the HRTEM images (**Figure 1b**). The d-spacings were
172 estimated at 0.49 and 0.31 nm, which were assigned to the (111) and (110) facets for the MCO
173 catalysts and were larger than the d-spacings of pristine ceria (111) and (110) of 0.31 and 0.19
174 nm, respectively (**SI Figure S4**). In coordination with the downward shift profile of the
175 corresponding XRD peaks, the increase in d-spacings was associated with the formation of the
176 defect sites (e.g., oxygen vacancies or Ce^{4+} reductions)[17, 22] within the MCO samples (**Figure**
177 **1c**). The crystal growth of MCO-001 along the [111] direction became predominant and led to
178 the formation of an irregular cylindrical shape with the exposed {001} facets[23]. MCO-001
179 exhibited a small diameter of approximately 30 nm, but it was much less stable than the two
180 other facets, because the crystal growth of the CeO_2 surfaces was quite fast in the [001] direction.

By contrast, the synthesis and control of high-quality crystal facet {001} were mostly dependent on organic ligand-assisted liquid-solid-solution phase synthetic transfer routes. Correspondingly, the selected-area electron diffraction pattern could be indexed as the diffraction spots in the (111) plane of MCO-111. Similarly, the two other MCO samples were exposed {110} and {001} facets. These observations could be compared with increased intensities of the diffraction peaks in the three exposed facets. Considering that the reversible Mn^{4+}–Mn^{3+} reduction transition is directly coupled with the localization/delocalization of the 4f electron of cerium, a high percentage of unsaturated atoms in the MnO_x−CeO_2 mixed oxides can possess superior reactivity. However, this effect could increase the challenge in engineering high-purity and well-defined crystal surfaces.

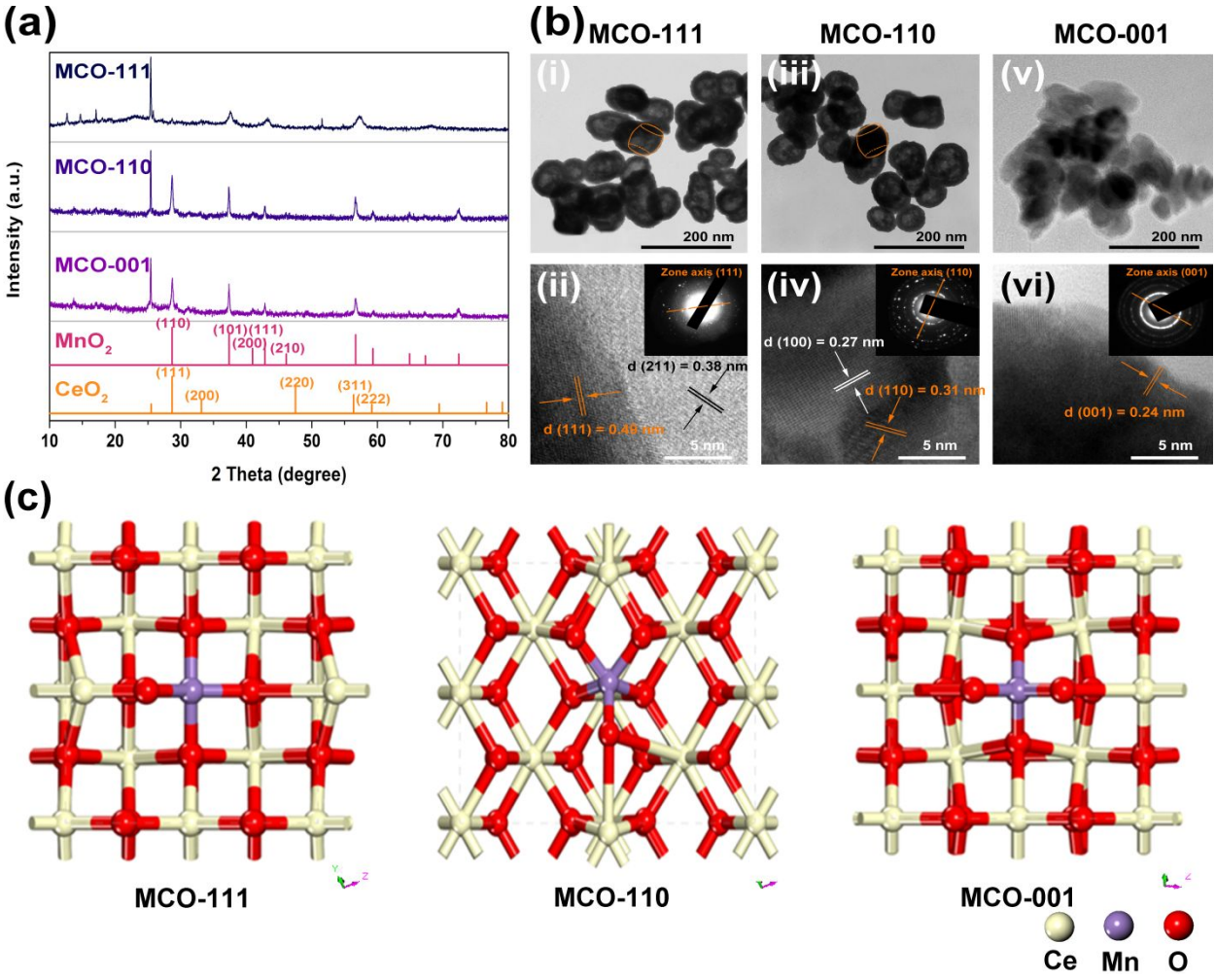

Figure 1. XRD patterns of pristine MnO_2, pristine CeO_2, and MCO catalysts with different exposed facets (a); TEM and HRTEM images of MCO catalysts with different exposed facets (b); and atomic structure of MCO-111, MCO-110, and MCO-001 (c).

TPR and TPD Profiles. Two reduction peaks were detected in a broad temperature range of 250 °C–500 °C, as shown in **Figure 2a**, indicating a reduction/oxidation cycle between transition-metal oxides with high valence and those with low valence during the ensuing redox loops of the oxidized Mn–Ce ions. By using ceria as oxygen carrier, oxygen migration was improved, and the redox-looping processes were replenished in the existence of mixed-valence Mn^{4+}–O–Mn^{3+} and Mn^{4+}–O–Ce^{4+}[2, 4]. These findings matched with the corresponding XPS results

(**SI Figures S5a–c**). In comparisons with the two other facets, the first reduction peak of MCO-111 moved to 267 °C, which corresponded to the consumption of surface oxygen species (O_{ads}), because the adsorbed oxygen species are easily dissociated on the catalyst surface[22]. The reduction of cerium and manganese ions did not largely result in a downward shift of the reduction peaks for all the three MCO samples. By contrast, more apparent downward shift to low temperatures of the two reduction peaks of MCO-111 was due to the continuous reduction of Mn^{4+} to Mn^{2+}[30, 31]. The intensities of the reduction peaks at low temperatures for MCO-111 were the highest, ascribing to the mobility of oxygen species and the generation of –OH species[30]. Larger mobility and consumption of lattice oxygen within MCO-111 were observed relative to MCO-110 and MCO-001. Mn^{4+} and Mn^{3+} were the two main Mn oxidation states in Mn 3s spectra obtained in **SI Figure S5b**. Hence, the contribution of the high-temperature peak to the total reduction profile was associated with the manganese ions with high oxidation states (Mn^{4+}) in the recycling redox loops. The central position of the reduction peaks of MCO-111 approached those of the reported Pt/MCO[9], whose catalytic activity often stands out from the majority of room-temperature catalytic oxidation (RCO) catalysts.

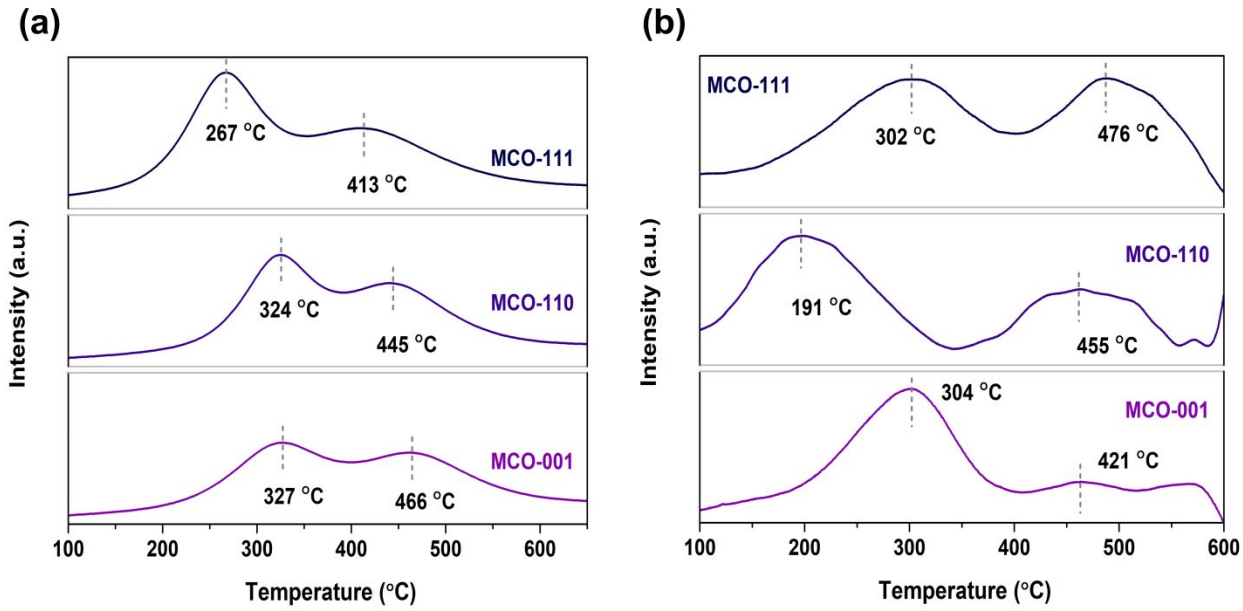

Figure 2. H_2–TPR (a) and O_2–TPD (b) profiles of MCO catalysts with different exposed facets.

The O_2–TPD spectra (**Figure 2b**) were analyzed to initially understand the roles of oxygen species within the different exposed facets, which corresponded to the formation of oxygen vacancies and subsequently access the HCHO oxidation mechanisms. A large amount of O_2 desorbs from the catalyst at T<250 °C (denoted as α-O_2) and is ascribed to the physically adsorbed oxygen species, which are weakly bound to catalysts surfaces. The second desorption peak presented in 300 °C–500 °C range is denoted as β-O_2, which is correlated with surface non-stoichiometric oxygen desorption and reduction of Mn^{4+} to Mn^{3+}. The third stage of O_2 desorption at T>600 °C is named as γ-O_2, indicating that the remaining lattice oxygen species continue to decline, and high oxidation states in metal oxides are completely reduced at the high-temperature range[31-33]. Here, the O_2 desorption temperature of the three facets generally shifted toward the low-temperature region, indicating that the MCO catalysts were favorable in low-temperature activity stemming from the desirable BET performance and bulk lattice oxygen migration of cerium-based oxygen carriers[18, 22]. The adsorbed O_2 could be readily transformed

into atomic oxygen (O*) and continue to form surface active oxygen (O^- and O_2^-) at the catalyst surfaces[30]. A large amount of oxygen adsorption and migration at low temperature could benefit the conversion of O_2 into O*, leading to HCHO oxidation. MCO-110 possessed strong O_2 desorption at the α-O_2 peak range, which corresponded to the increased formation of oxygen vacancies on the surface relative to MCO-111 and MCO-001 and were consistent with the corresponding O 1s XPS spectra (**SI Figure S5d**).

RCO Activity and Selectivity. Figure 3a shows the turnover frequencies (TOFs) per unit of surface area ($mol_{HCHO} \cdot s^{-1} \cdot m_{cat}^{-2}$) over the MCO with different exposed facets. Under a GHSV of 4×10^4 h^{-1}, the activities presented facet dependence and followed the sequence of MCO-111>MCO-110>MCO-001. The TOFs of MCO-111 of approximately 7.5×10^{-4} $\mu mol \cdot s^{-1} \cdot m^{-2}$ at a low temperature range of 25 °C–45 °C were higher than those of MCO-110 (approximately 4.5×10^{-4} $\mu mol \cdot s^{-1} \cdot m^{-2}$) and MCO-001 ($3.0 \times 10^{-4}$ $\mu mol \cdot s^{-1} \cdot m^{-2}$). In comparison with some typical transition metal-based catalysts in **SI Table S4**, the temperatures for complete HCHO oxidation must exceed 70 °C. The increase in reaction temperature can increase the selectivity toward CO_2 and decrease the production of formic acid intermediates[9]. The TOFs of MCO-111 and MCO-110 catalysts at low temperatures were parallel with those of reported transition metal oxides at high temperatures. The catalytic activity of MCO-111 even approached that of some Ag-supported catalysts[34, 35]. Notably, noble metal-supported catalysts (e.g., Pt/TiO_2[36] and Pd/TiO_2[37]) can result in complete HCHO conversion at near-room temperature. Considering the limitations in the scaling-up cost and mass dispersion control of the noble metal, transition metal oxides may be promising substitutes if lattice defects or oxygen vacancies are engineered to act as additional active sites. The recycling activity and stability of MCO with the different exposed facets were determined in **Figure 3b**. MCO-111 converted 56% HCHO into CO_2 at 35 °C, followed by

MCO-110 (50%) and MCO-001 (42%). No apparent deactivation was observed in 360 min reaction periods. In addition, the half reaction time ($t_{50\%}$) was independent on the initial reactant concentration (**SI Figure S6**), suggesting that HCHO catalytic oxidation followed a pseudo-first-order reaction and the RCO system could be adapted to HCHO removal at the sub-ppm level[38, 39].

Oxygen vacancy sites are responsible for adsorption and catalytic activity. Interestingly, the formation of oxygen vacancies was feasible on the {110} and {001} facets but did not incur comparatively high activity **(Figure 3**). Except for the distorted electronic structure of crystals with different exposed facets, the activity was also influenced by the migration of definite surface oxygen and stability of the formed oxygen vacancies[22]. The quantitative effects of oxygen vacancies regarding to oxygen storage capacity are analyzed to demonstrate the migration of bulk lattice oxygen in the following section.

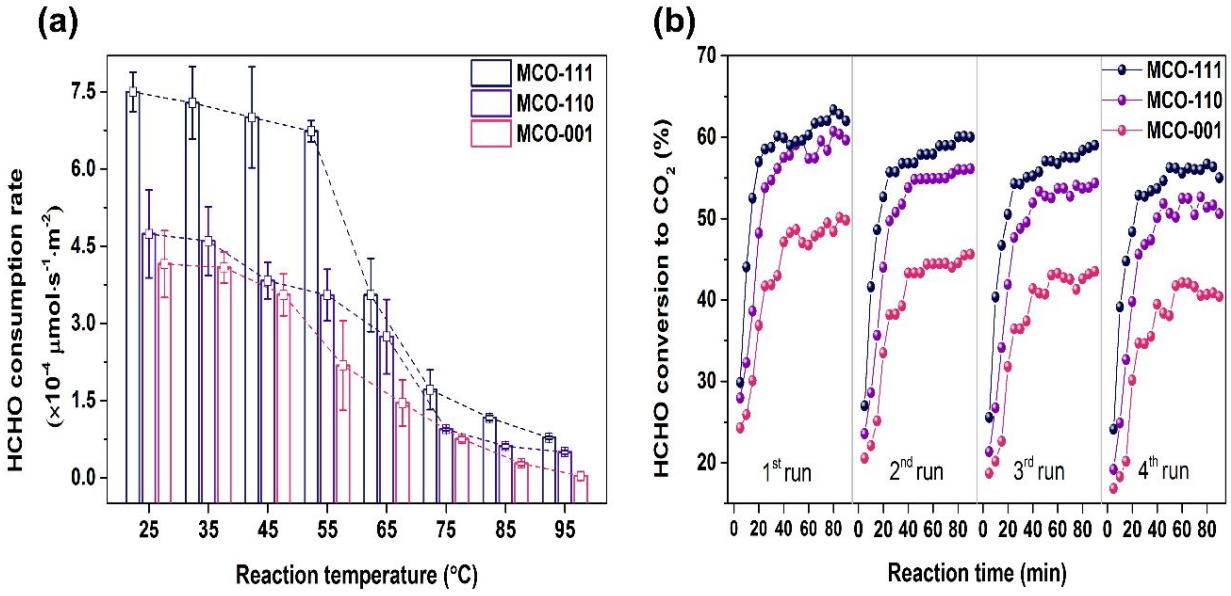

Figure 3. HCHO consumption rate as a function of reaction temperature (a) and recycling catalytic activity and stability in 90 min of each run (b) over MCO catalysts with different exposed facets at 35 °C

Quantitative Effects of Oxygen Vacancies. The oxygen vacancy defects were engineered to work as active centers that were correlated with adsorption, catalytic activity, and stability. The O_2–TPD and O 1s XPS studies roughly demonstrated oxygen speciation in the chemical-looping processes of metal oxides but failed to clearly elucidate the roles and oxygen storage capacity of definite lattice oxygen, i.e., surface lattice oxygen O_{S-L} and bulk lattice oxygen O_{B-L}[22]. The surface lattice oxygen (O_{S-L}), rather than the surface adsorbed oxygen, was found to be responsible for the catalytic activity and replenished from the migration of bulk lattice oxygen[22]. Understanding the quantitative effects of oxygen species is of practical importance in the catalyst design based on high-performance oxygen carriers. The correlation between the migration and consumption of lattice oxygen and the formation of oxygen vacancies within the exposed facets was investigated through the designed H_2–TPR experiments.

The corresponding H_2 consumption amounts of O_{B-L} at 600 °C for different treatment times are summarized in **SI Table S5**. The H_2 consumption amount of O_{B-L} was approaching to a minimum level when the MCO samples were treated for more than 5 h. MCO-110 had the lowest H_2 consumption during the whole treatment, which was correlated with the formation of the maximum oxygen vacancies within MCO-110 obtained in the O_2–TPD profiles (**Figure 2b**). The corresponding migration rate was the slowest at 8.0×10^{-3} $\mu mol \cdot g^{-1} \cdot s^{-1}$. The fastest migration rate up to 1.1×10^{-2} $\mu mol \cdot g^{-1} \cdot s^{-1}$ was found for MCO-001 but failed to result in the highest catalytic activity, because the {001} facet growth was somewhat suppressed by the ceria (111) and (200) planes[23]. Oxygen vacancies were more stable within pristine ceria {111} facet than within pristine ceria {110} and {001}, they occurred more easily within the {110} and {001} though[16, 18]. Aside from the stable defect structure of crystal facet, improvements in catalytic activity were ascribed to the fact that the O_{B-L} mobility at faster migration rate can replenish O_{S-L},

but the excessively fast rate within the {001} facet can decrease activity[22]. Oxygen vacancies could result in excellent catalytic activity and stability if they were more stable on catalyst surfaces.

As shown in **Table 1**, the designed H_2–TPR experiment at 450 °C was performed and examined at different treatment times to demonstrate the total consumption based on the migration of $O_{B–L}$ to $O_{S–L}$. The actual consumption rates of $O_{S–L}$ within MCO-111 were larger than those within MCO-110 and MCO-001 and remained stable after 5 h treatment relative to the migration rate of $O_{B–L}$. However, the consumptions of $O_{S–L}$ cannot be completely ruled out from the migration of $O_{B–L}$, possibly because of some mass loss in $O_{B–L}$ mobility. Thus, the largest consumption amounts of $O_{S–L}$ were not well associated with the largest consumption amounts of $O_{B–L}$. Therefore, $O_{B–L}$ through its faster migration can not only participate in the catalytic reaction but also replenish the consumed $O_{S–L}$. These events directly supported the importance of stable oxygen vacancies within the MCO-111 facet.

Table 1. H_2 consumption of $O_{B–L}$ and $O_{S–L}$ of MCO samples treated at 450 °C with 10% H_2/Ar for different treatment times.

Samples	H_2 consumption of $O_{B–L}$ ($\mu mol \cdot g^{-1}$)	H_2 consumption of $O_{S–L}$ ($\mu mol \cdot g^{-1}$) [a]	$O_{B–L}$ migration ($\mu mol \cdot g^{-1}$)	$O_{S–L}$ consumption ($\mu mol \cdot g^{-1}$) [b]	Actual consumption rate of $O_{S–L}$ ($\mu mol \cdot g^{-1} \cdot s^{-1}$) [c]
Untreated MCO-111	645	568	0	0	0
Untreated MCO-110	549	516	0	0	0
Untreated MCO-001	676	593	0	0	0
Treated MCO-111 (1 h)	633	409	6	79.5	2.0×10^{-2}

Treated MCO-110 (1 h)	539	373	5	71.5	1.8×10^{-2}
Treated MCO-001 (1 h)	661	441	7.5	76	1.9×10^{-2}
Treated MCO-111 (5 h)	315	166	165	201	2.0×10^{-3}
Treated MCO-110 (5 h)	241	159	154	178.5	1.4×10^{-3}
Treated MCO-001 (5 h)	279	163	198.5	215	0.9×10^{-3}

[a] H_2 consumption of O_{S-L} was calculated according to TPR profiles at temperature range of 300 °C–600 °C.

[b] Consumption amount of O_{S-L} = (H_2 consumption of untreated sample−H_2 consumption of treated sample)/2.

[c] Actual consumption rate of O_{S-L} = (consumption amount of O_{S-L}−migration amount of O_{B-L})/treatment time.

Identification of Catalytically Active Regions and Active-Site Behaviors at Low Temperatures. The activation of oxygen species and catalytic oxidation are favorable to high reaction temperatures. However, the performance of the temperature-dependent catalysts that can trigger their activity at low temperatures has been rarely studied. Here high-throughput screening studies with IR thermography were performed to distinguish and identify catalytically active regions[24, 25]. As shown in **Figure 4**, the catalytically active regions corresponding to temperature variations were characterized and compared in various isothermal feeds. First, the IR absorbance intensities of the different exposed facets were obtained from 25 °C–175 °C, which were closely consistent with different surface active regions at varying feed temperatures **(Figure 4a)**. The IR absorbance was monitored under the average of the emerging temperatures when a hot spot region of IR thermography was formed on the catalyst surfaces. Small changes in the IR absorbance were observed in a high temperature range of 125 °C–175 °C, despite a gradual

decline with increasing feed temperatures. Moreover, no huge difference in the IR absorbance and retention was found among the three exposed facets at the high-temperature range. Below 75°C, comparatively large IR absorbance intensities were attained at MCO-111 compared with MCO-110 and MCO-001. MCO-111 maintained enhanced intensity and retention of the IR absorbance under the emerging temperatures at 25 °C–50 °C. The IR thermography images were then recorded to visualize the active regions at low temperatures after the emerging temperature reached 50 °C in **Figure 4b**. The amplitude (i.e., retention of the maximum emerging temperature after hot spot formation) of the temperature gradient could be clearly compared at the different crystal facets. The amplitude of the maximum temperature gradient was broader and stronger at MCO-111 than at the two other facets, although the IR absorbance was released and extinguished during cooling to 25°C. The highly active zones displayed at MCO-111 could act as a reactive catalytic bed to sustain the exposure of abundant active sites and participation of oxygen species at low temperatures, thereby providing the enhanced catalytic activity of MCO-111 under ambient conditions.

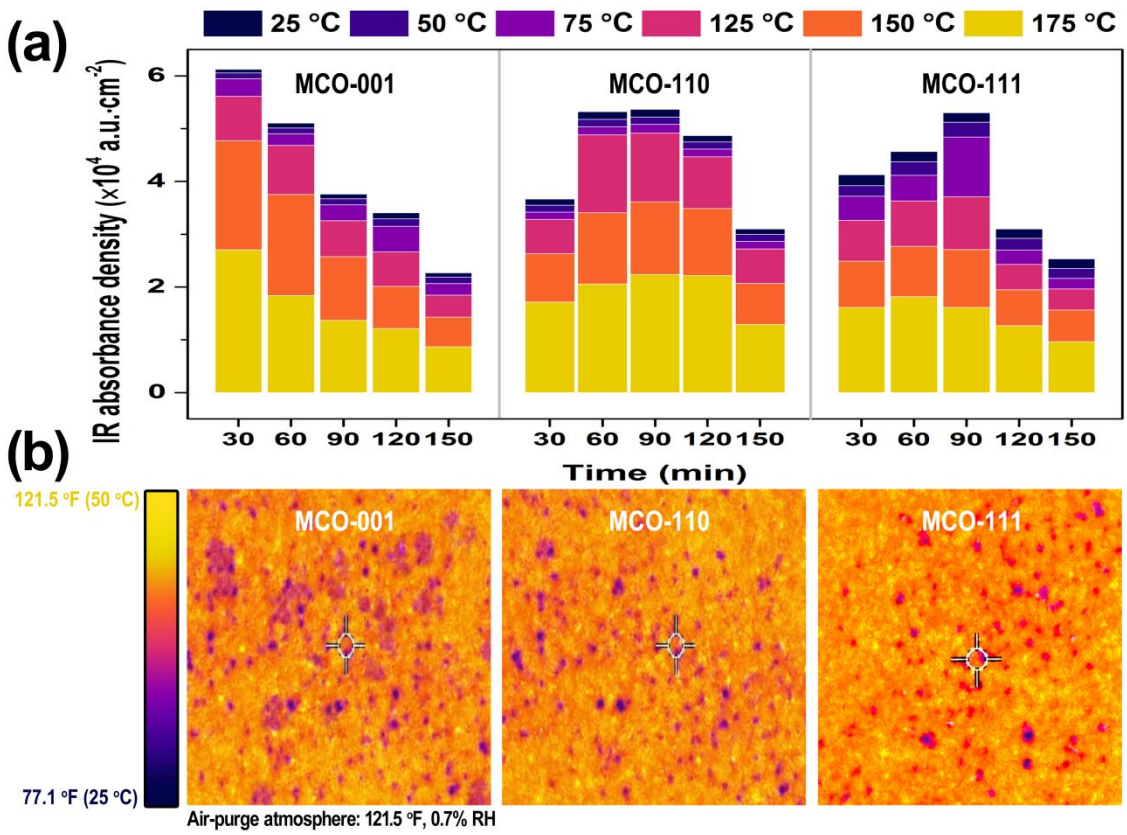

Figure 4. IR absorbance intensities of MCO catalysts with different exposed facets at varying feed temperatures from 25 °C to 175 °C (a) and identification of catalytically active zones after the emerging temperatures reached 50 °C via IR thermography images (b).

The types and properties of surface active sites at different exposed facets were investigated through Py-IR measurements[40, 41]. Metal oxides are used for their acid–base properties. Two kinds of surface metal sites, i.e., Lewis acid (L-acid) and Brønsted acid (B-acid) sites, are related to free electron and proton exchange at metal oxides. For transition-metal oxides, the Lewis acid–base properties depend on cyclic electron transfer in the chemical-looping processes and play a major role in the activation of reactive oxygen species[42]. As shown in **Figures 5**, the peaks at *ca.* 1456 and 1610 cm^{-1} bands originated from pyridine adsorbed onto L-acid sites, whereas the peaks at *ca.* 1545 and 1635 cm^{-1} bands were related to B-acid sites. The peak at *ca.* 1489 cm^{-1} originated from pyridine adsorbed onto L-acid and B-acid sites. The exposure of

predominant L-acid sites was observed at the three major exposed facets. The Lewis/Brønsted (L/B) ratio at MCO-111 was 2.85 larger than that at MCO-110 and MCO-001 with 2.11 and 1.94, respectively. A high degree of nucleophilic substitution was assigned to an exchange of surface metal sites and atomic O*, and the hopping of hydrocarbon compounds to atomic O* was preferential onto L-acid sites. B-acid sites acted as predominant active sites in favor of high reaction temperatures[43]. Furthermore, the exposure of L-acid and B-acid sites was influenced by high ambient humidity[40, 41]. However, many routine metallic catalysts were water-repellent that affects HCHO adsorption and catalytic oxidation under ambient conditions to a certain extent. Therefore, Lewis acid sites involving the superior selective adsorption of electrolyte cations were presented for polar HCHO molecules induced by cyclic electron transfer. The acid–base properties provided explicit evidence of strength and distribution of surface-active sites. The predominance of L-acid sites at low temperatures could facilitate the activation of surface oxygen species to reactive oxygen species and catalytic activity of RCO catalysts.

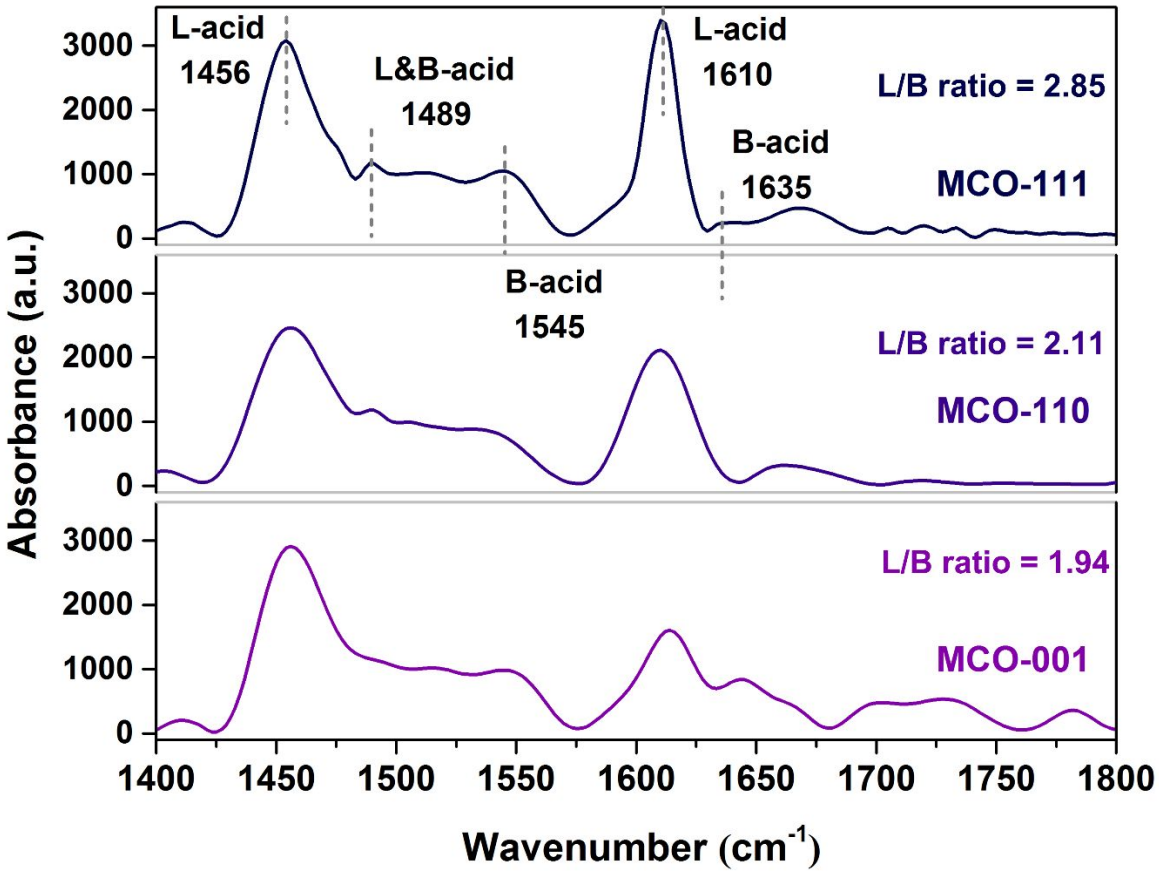

Figure 5. Py-IR measurements of acid–base active sites at MCO with different exposed facets.

***In Situ* XPS and DRIFT Studies.** The adsorption and reaction of HCHO over MCO catalysts with different exposed facets were studied using *in situ* C 1s XPS measurements. As shown in **Figure 6a**, the XPS peaks in the C 1s region were more precisely deconvoluted to adventitious carbon (C_A) at 284.5 eV from C–C species and at 285.5 eV from C–O–C species, to formaldehyde/mono-dentate formate species (C_F) at 288.2 eV, and O–C=O (carboxylate species = C_{CB}) at 289.1 eV[44, 45]. These peaks were consistent with the assignment of chemical bonds to the BE of C 1s peaks in **SI Table S2**. C_F signals were retained on the three exposed facets, and more evolutions of C_A were found for MCO-111. The C 1s core level envelope presented an important contribution at the BE of C_F at temperatures below 50 °C. The intensities of C_{CB}

photopeaks were lower than those of C_F and C_A photopeaks for the three samples. The formation of C_A favored increased reaction temperatures, which was preferential to CO oxidation and CO_2 yield. Both formaldehyde and formate species were bonded end-on through the oxygen atom, and the rapid conversion of C_{CB} species continued. Therefore, physisorption was an initial preadsorption step, chemisorption started with physisorption, and the strong interaction between the adsorbate and sorbent surface created new types of electronic bonds (ionic or covalent). The chemisorption and oxidation of HCHO were derived from H bonding of formaldehyde and formate groups and bridging of C_{CB} preferentially with oxygen atom in the MCO surfaces[41, 46]. These findings matched well with the quantitative effects of oxygen vacancies in which excess defects could not sustain the oxygen species-oriented active sites involved in the adsorption and oxidation.

The formation of intermediate species for HCHO decomposition at 35 °C was examined through *in situ* DRIFT spectra (**Figure 6b**). All transient reaction results represented the main intermediates that were ascribed to formate species (including carboxylate), carbonate, CO_2, and water vapor. The absorbance intensities of the CO_2 peak (*ca.* 2380 cm^{-1}) and surface hydroxyl species (a broad OH stretching region located at *ca.* 3580 cm^{-1}, denoted as υ_s [OH]) increased significantly for MCO-111 compared with exposure of MCO-110 and MCO-001 to $HCHO/O_2$. The symmetric stretching OH possesses a strongly hydrogen bonded water structure and could facilitate the chemisorption of HCHO in terms of hydroxyl bonding preferable with the methyl groups under low temperature and relative humidity[41]. MCO-111 achieved comparatively high catalytic activity for HCHO conversion, producing CO_2 and water vapor as final products. In brief, HCHO peaks (*ca.* 1680 cm^{-1}) weakened with reaction time and new typical bands indicated the gradual generation of formate species (quite weak at *ca.* 2840 cm^{-1} for υ_s [CH], *ca.*

1466 cm^{-1} for δ [CH_2], *ca.* 1601 cm^{-1} for υ_s [COO], and *ca.* 1350 and 1314 cm^{-1} for υ_{as} [COO])[46, 47]. The decomposition of –COO and –CH_2 species resulted from the nucleophilic attack of the reactive oxygen atom. The intensities of –CH_2 and –OH were stronger than those of the –CH match. In fact, the ensuing conversions from the intermediate CH_2OO are more complex than those from HCHO initially, because distinct and complex chemical speciation and reactivity pathways of the CH_2OO isomers (i.e., formic acid, dioxirane, and CH_2OO Criegee) have been found[41]. The conversions of HCHO into formic acid and dioxirane preferentially occur through monodentate binding and bidentate coordination with metal sites of catalysts, respectively. The production and removal of CH_2OO Criegee are rather complex and probably involved in side or secondary processes. CH_2OO Criegee has some single bond characters, which are assumed to a rapid dissociation of C–C and O–O bonds from the oxidation of unsaturated carboxyl groups.

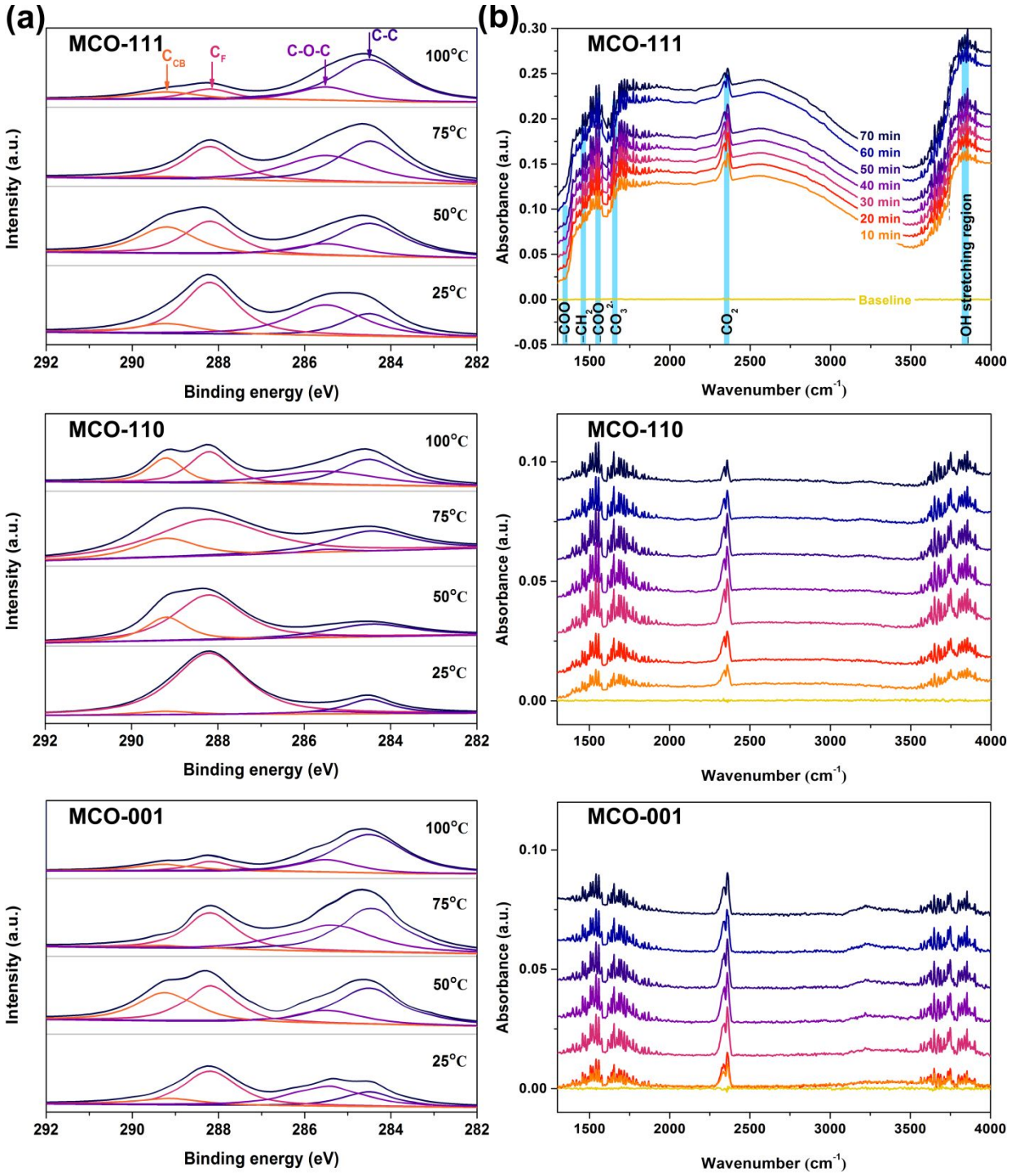

412

413 **Figure 6.** *In situ* C 1s XP spectra as a function of reaction temperature of the HCHO-exposed

414 MCO catalysts with different exposed facets (a) and *in situ* DRIFT spectra of bond cleavage at

415 35 °C (b).

416 **Practical Application in Household Air Cleaner and In-field Pilot Test.** MnO_x–CeO_2

417 samples with the exposed {111} facet were examined with respect to room-temperature catalytic
418 activity in laboratory scale and were about to be validated in an in-field test for actual HCHO
419 removal. First, a prototype of a household air cleaner was designed and equipped with a filter
420 cylinder cartridge in **Figure 7**, whose main dimensions and operating parameters are listed in **SI**
421 **Table S6**. The cylinder cartridge consisted of five sets of porous filtration units, that is, non-
422 woven fabric filter, high efficiency particulate air (HEPA) filter, two layers of nylon fabric filter,
423 and polytetrafluoroethylene (PTFE) keel shirt, and operated through outside-in filtration. Test
424 MCO-111 particles in a sieve fraction of 140 meshes (approximately 106 μm) were scaled-up
425 and immobilized with a loading density of approximately 0.30 $g \cdot cm^{-2}$ between two layers of
426 nylon fabric filter. The fabric filter mainly removed fine particulate matter and priority gaseous
427 pollutants in indoor air (e.g., HCHO and NO_x). Airflow was controlled with a built-in air pump
428 (maximum airflow, 400 $m^3 \cdot h^{-1}$), and purified air was released from the outlet at the top of the air
429 cleaner. After the majority of particulate matter was pre-filtered through the multi-layer
430 filtration, gaseous pollutants were in contact with the catalyst and then oxidized into harmless
431 substances under ambient conditions.

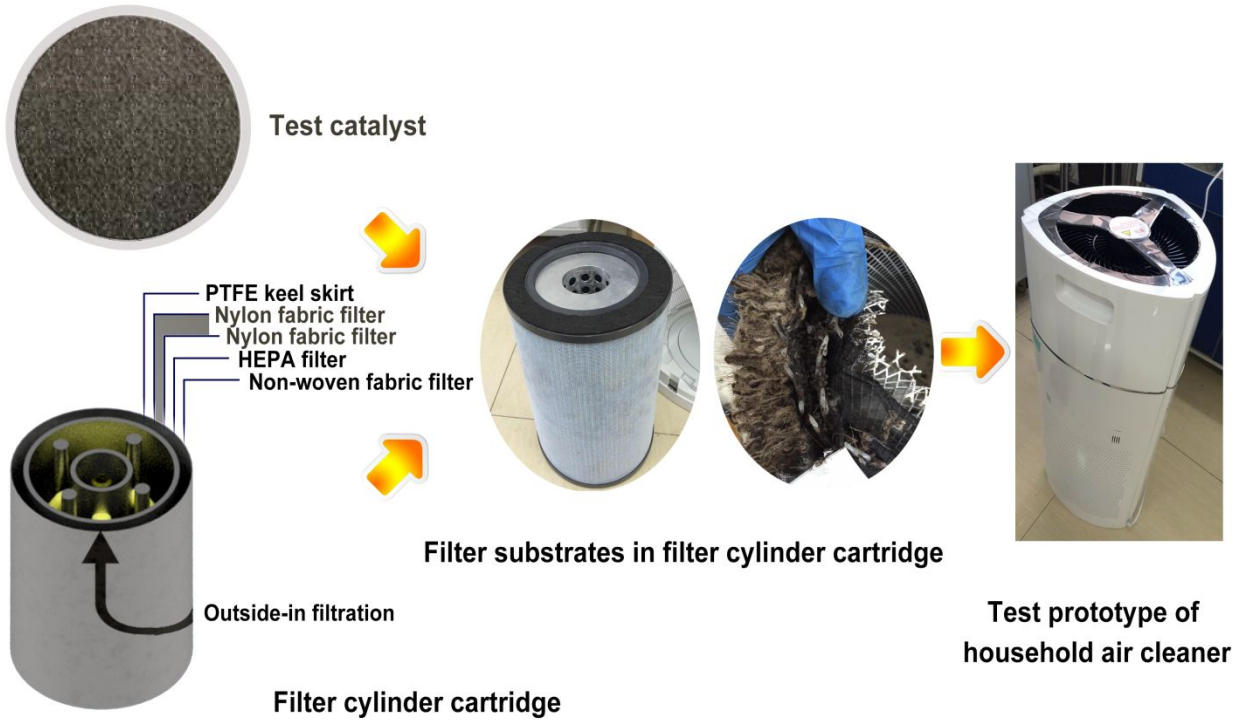

Figure 7. Scaling-up MCO-111 filter substrates filled in the filter cylinder cartridge of a household air cleaner.

To evaluate the HCHO removal efficiency of the MCO-111 catalyst, we conducted an in-field pilot test of the household air cleaner at a newly decorated office, as shown in **Figure 8**. The concentration of HCHO during a round switch on and off of the air cleaner was continuously measured using a portable analyzer (Interscan 4160, USA) and double-checked in the on-site measurement for 5 days. According to the air cleaner standard (GB/T 18801–2015, China), the sampling inlet of the analyzer was kept at a vertical distance higher than 0.8 m with the ground and a horizontal distance of 1.75 m from the purified air outlet of the air cleaner in a 30 m^3 test site. When the air cleaner started to work, the concentration of HCHO dramatically decreased and remained as low as 20 ppb over an 8 h period, which stratified with the Excellent Class (30 $\mu g \cdot m^{-3}$, equal with std. 24 ppb of an 8 h average) of Indoor Air Quality Certification Scheme for Offices and Public Places issued in Hong Kong. By contrast, when switched off, the

concentration of HCHO gradually recovered to its initial level at approximately 120 ppb, exceeding a maximum exposure of 100 ppb (equal with std. 81 ppb of an 8 h average) indoors. HCHO emissions in indoor air are long-lasting and result from a source complex, such as building materials, furnishings, and occupant activities. The situation is aggravated during a lack of ventilation in most enclosed areas, thereby seriously burdening long-term removal efficiency. The routine household air cleaner, mainly equipped with porous-media filters, shows a very insufficient ability in removing gaseous pollutants. A very few commercial air cleaners are available in the combined use between catalytic oxidation and mechanical filtration. Therefore, the test MCO-111 catalyst can work synergically to optimize and maximize the air cleaner performance for the removal of HCHO. Furthermore, this work has a proper strategy recommendation for translating laboratory research into commercial value in large scale to eliminate HCHO in indoor air via the efficient and cost-effective catalytic oxidation to attain the standard protocols of indoor air quality.

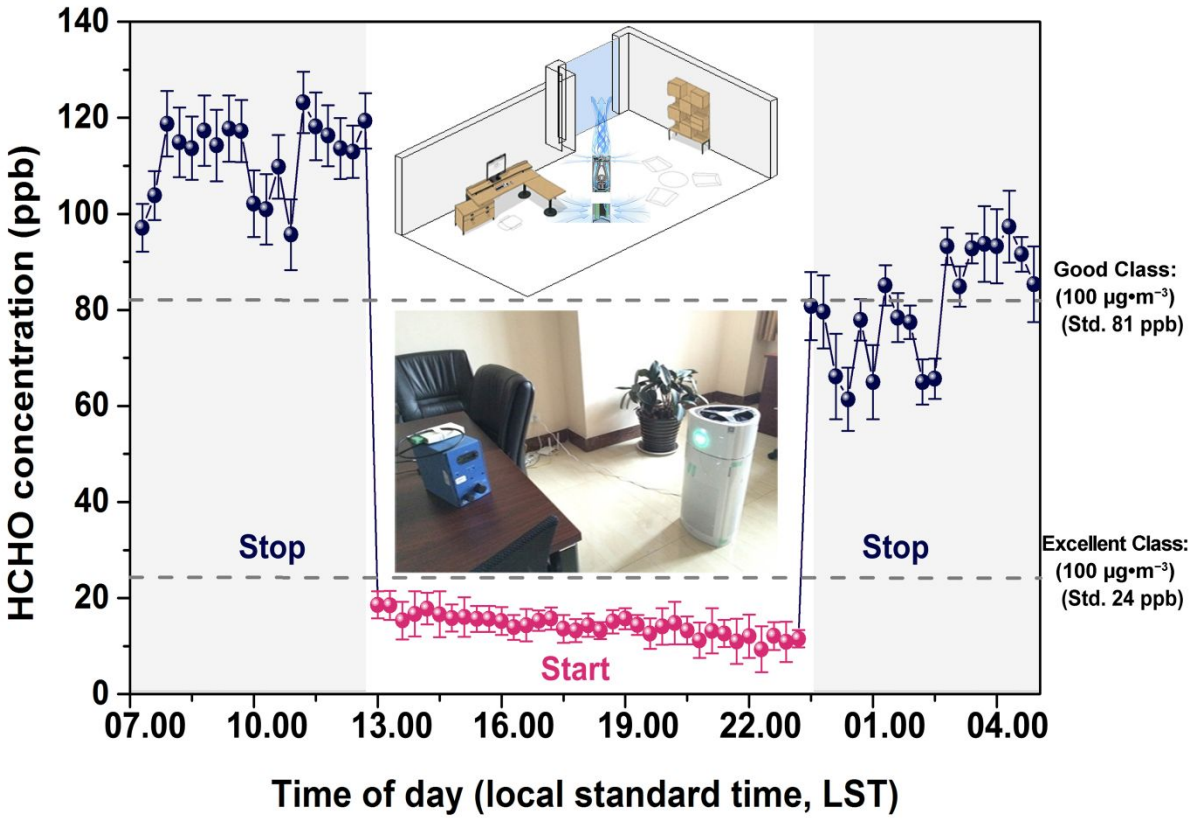

Figure 8. In-filed pilot test of the household air cleaner for HCHO removal in 5 days. Inset photo images: on-site measurements at a newly decorated office (approximately 30 m^3) without ventilation.

ASSOCIATED CONTENT

Supporting Information. The Supporting Information associated with this article can be found in this section, including the detailed methods of characterizations by H_2–TPR, O_2–TPD, Py-IR, infrared thermography, *in situ* XPS and DRIFT, catalytic activity measurement, assignment of chemical bonds to BEs of C 1s peaks, BET performance, TGA of MCO-111, TEM and HRTEM of precursor ceria {111} and {110}, survey of catalytic activity for HCHO oxidation over typical RCO catalysts, migration of O_{B-L}, high-resolution XPS spectra, determination of the half reaction time ($t_{50\%}$), and specification of the filter cylinder cartridge in a test prototype of the

household air cleaner.

AUTHOR INFORMATION

Corresponding Authors

*Prof. Shun-cheng Lee (Email: ceslee@polyu.edu.hk)

*Prof. Yu Huang (Email: huangyu@ieecas.cn)

Notes

The authors declare no competing interests.

Acknowledgements

This work was supported by the National Key Research and Development Program of China (2016YFA0203000), the Research Grants Council of Hong Kong Government (Project No. T24/504/17), the Research Grants Council of Hong Kong Government (Project No. PolyU152083/14E, PolyU152090/15E, and 18301117), and the Hong Kong RGC Collaborative Research Fund (C5022-14G). Yu Huang was also supported by the "Hundred Talent Program" of the Chinese Academy of Sciences.

REFERENCES

(1) Quiroz Torres, J.; Royer, S.; Bellat, J. P.; Giraudon, J. M.; Lamonier, J. F., Formaldehyde: catalytic oxidation as a promising soft way of elimination. *ChemSusChem* **2013,** *6*, (4), 578–592.

(2) Quiroz, J.; Giraudon, J. M.; Gervasini, A.; Dujardin, C.; Lancelot, C.; Trentesaux, M.; Lamonier, J. F., Total oxidation of formaldehyde over MnO_x–CeO_2 catalysts: the effect of acid treatment. *ACS Catal.* **2015,** *5*, 2260–2269.

(3) Wang, J.; Li, J.; Jiang, C.; Zhou, P.; Zhang, P.; Yu, J., The effect of manganese vacancy in birnessite-type MnO_2 on room-temperature oxidation of formaldehyde in air. *Appl. Catal. B: Environ.* **2017,** *204*, 147–155.

(4) Li, H.; Huang, T.; Lu, Y.; Cui, L.; Wang, Z.; Zhang, C.; Lee, S.; Huang, Y.; Cao, J.; Ho, W., Unraveling the mechanisms of room-temperature catalytic degradation of indoor formaldehyde and its biocompatibility on colloidal TiO_2-supported MnO_x–CeO_2. *Environ. Sci-Nano* **2018,** *5*, (5), 1130–1139.

(5) Wang, C.; Wen, C.; Lauterbach, J.; Sasmaz, E., Superior oxygen transfer ability of Pd/MnO_x–CeO_2 for enhanced low temperature CO oxidation activity. *Appl. Catal. B-Environ.* **2017,** *206*, 1–8.

(6) Zha, K.; Cai, S.; Hu, H.; Li, H.; Yan, T.; Shi, L.; Zhang, D., In Situ DRIFTs Investigation of Promotional Effects of Tungsten on MnO_x–CeO_2/meso-TiO_2 Catalysts for NO_x Reduction. *J. Phys. Chem. C* **2017,** *121*, (45), 25243–25254.

(7) Zhang, L.; Zhang, D.; Zhang, J.; Cai, S.; Fang, C.; Huang, L.; Li, H.; Gao, R.; Shi, L., Design of meso-TiO_2@MnO_x–CeO_x/CNTs with a core-shell structure as $DeNO_x$ catalysts: promotion of activity, stability and SO_2-tolerance. *Nanoscale* **2013,** *5*, (20), 9821–9829.

(8) Tang, X.; Chen, J.; Li, Y.; Li, Y.; Xu, Y.; Shen, W., Complete oxidation of formaldehyde over Ag/MnO_x–CeO_2 catalysts. *Chem. Eng. J.* **2006,** *118*, (1–2), 119–125.

(9) Tang, X.; Chen, J.; Huang, X.; Xu, Y.; Shen, W., Pt/MnO_x–CeO_2 catalysts for the complete oxidation of formaldehyde at ambient temperature. *Appl. Catal. B-Environ.* **2008,** *81*, (1), 115–121.

(10) Miao, L.; Wang, J.; Zhang, P., Review on manganese dioxide for catalytic oxidation of airborne formaldehyde. *Appl. Surf. Sci.* **2018,** *466*, 441–453.

(11) Rong, S.; Zhang, P.; Liu, F.; Yang, Y., Engineering crystal facet of α-MnO_2 nanowire for highly efficient catalytic oxidation of carcinogenic airborne formaldehyde. *ACS Catal.* **2018,** *8*, (4), 3435–3446.

(12) Weon, S.; Choi, E.; Kim, H.; Kim, J. Y.; Park, H.-J.; Kim, S.-m.; Kim, W.; Choi, W., Active {001} facet exposed TiO_2 nanotubes photocatalyst filter for volatile organic compounds removal: from material development to commercial indoor air cleaner application. *Environ. Sci. Technol.* **2018,** *52*, (16), 9330–9340.

(13) Patnaik, S.; Sahoo, D. P.; Mohapatra, L.; Martha, S.; Parida, K., $ZnCr_2O_4$@ ZnO/g-C_3N_4: a triple-junction nanostructured material for effective hydrogen and oxygen evolution under visible light. *Energy Technol.* **2017,** *5*, (9), 1687–1701.

(14) Ali, A. M.; Daous, M. A.; Khamis, A. A.; Driss, H.; Burch, R.; Petrov, L. A., Strong synergism between gold and manganese in an Au–Mn/triple-oxide-support (TOS) oxidation catalyst. *Appl. Catal. A-Gen.* **2015,** *489*, 24–31.

(15) Xu, H.; Yan, N.; Qu, Z.; Liu, W.; Mei, J.; Huang, W.; Zhao, S., Gaseous heterogeneous catalytic reactions over Mn-Based oxides for environmental applications: a critical review. *Environ. Sci. Technol.* **2017,** *51*, (16), 8879–8892.

(16) Esch, F.; Fabris, S.; Zhou, L.; Montini, T.; Africh, C.; Fornasiero, P.; Comelli, G.; Rosei, R., Electron localization determines defect formation on ceria substrates. *Science* **2005,** *309*, (5735), 752–755.

(17) Sudarsanam, P.; Hillary, B.; Amin, M. H.; Hamid, S. B. A.; Bhargava, S. K., Structure-activity relationships of nanoscale MnO_x/CeO_2 heterostructured catalysts for selective oxidation of amines under eco-friendly conditions. *Appl. Catal. B-Environ.* **2016,** *185*, 213–224.

(18) Sun, C.; Li, H.; Chen, L., Nanostructured ceria-based materials: synthesis, properties, and applications. *Energ. Environ. Sci.* **2012,** *5*, (9), 8475–8505.

(19) Zhang, D.; Du, X.; Shi, L.; Gao, R., Shape-controlled synthesis and catalytic application of ceria nanomaterials. *Dalton T.* **2012,** *41*, (48), 14455–14475.

(20) Wang, J.; Sun, J.; Jing, Q.; Liu, B.; Zhang, H.; Yongsheng, Y.; Yuan, J.; Dong, S.; Zhou, X.; Cao, X., Phase stability and thermo-physical properties of ZrO_2–CeO_2–TiO_2 ceramics for thermal barrier coatings. *J. Eur. Ceram. Soc.* **2018,** *38*, (7), 2841–2850.

(21) Xiong, Y.; Tang, C.; Yao, X.; Zhang, L.; Li, L.; Wang, X.; Deng, Y.; Gao, F.; Dong, L., Effect of metal ions doping (M = Ti^{4+}, Sn^{4+}) on the catalytic performance of MnO_x/CeO_2 catalyst for low temperature selective catalytic reduction of NO with NH_3. *Appl. Catal. A-Gen.* **2015,** *495*, 206–216.

(22) Chen, D.; He, D.; Lu, J.; Zhong, L.; Liu, F.; Liu, J.; Yu, J.; Wan, G.; He, S.; Luo, Y., Investigation of the role of surface lattice oxygen and bulk lattice oxygen migration of cerium-based oxygen carriers: XPS and designed H_2–TPR characterization. *Appl. Catal. B-Environ.* **2017,** *218*, 249–259.

(23) Zhang, J.; Ohara, S.; Umetsu, M.; Naka, T.; Hatakeyama, Y.; Adschiri, T., Colloidal ceria

554 nanocrystals: a tailor-made crystal morphology in supercritical water. *Adv. Mater.* **2007,** *19*,
555 (2), 203–206.
556 (24) Gänzler, A. M.; Casapu, M.; Boubnov, A.; Müller, O.; Conrad, S.; Lichtenberg, H.; Frahm,
557 R.; Grunwaldt, J.-D., Operando spatially and time-resolved X-ray absorption spectroscopy
558 and infrared thermography during oscillatory CO oxidation. *J. Catal.* **2015,** *328*, 216–224.
559 (25) Ramirez, A.; Hueso, J. L.; Mallada, R.; Santamaria, J., In situ temperature measurements in
560 microwave-heated gas-solid catalytic systems. Detection of hot spots and solid-fluid
561 temperature gradients in the ethylene epoxidation reaction. *Chem. Eng. J.* **2017,** *316*, 50–60.
562 (26) Abdul-Wahab, S. A.; En, S. C. F.; Elkamel, A.; Ahmadi, L.; Yetilmezsoy, K., A review of
563 standards and guidelines set by international bodies for the parameters of indoor air quality.
564 *Atmos. Pollut. Res.* **2015,** *6*, (5), 751–767.
565 (27) Burnett, J., Indoor air quality certification scheme for Hong Kong buildings. *Indoor Built*
566 *Environ.* **2005,** *14*, (3–4), 201–208.
567 (28) Huang, Y.; Wang, W.; Zhang, Y.; Cao, J.; Huang, R.; Wang, X., Synthesis and applications
568 of nanomaterials with high photocatalytic activity on air purification. In *Novel*
569 *Nanomaterials for Biomedical, Environmental and Energy Applications*, Elsevier: 2019; pp
570 299–325.
571 (29) Huang, Y.; Wang, P.; Wang, Z.; Rao, Y.; Cao, J.-j.; Pu, S.; Ho, W.; Lee, S. C., Protonated g-
572 C_3N_4/Ti^{3+} self-doped TiO_2 nanocomposite films: room-temperature preparation,
573 hydrophilicity, and application for photocatalytic NO_x removal. *Appl. Catal. B-Environ.*
574 **2019,** *240*, 122–131.
575 (30) Wang, J.; Zhang, P.; Li, J.; Jiang, C.; Yunus, R.; Kim, J., Room-temperature oxidation of
576 formaldehyde by layered manganese oxide: effect of water. *Environ. Sci. Technol.* **2015,** *49*,

(20), 12372–12379.

(31) Zhang, T.; Li, H.; Yang, Z.; Cao, F.; Li, L.; Chen, H.; Liu, H.; Xiong, K.; Wu, J.; Hong, Z., Electrospun YMn_2O_5 nanofibers: a highly catalytic activity for NO oxidation. *Appl. Catal. B-Environ.* **2019,** *247*, 133–141.

(32) Lee, Y. N.; Lago, R. M.; Fierro, J. L. G.; Cortés, V.; Sapiña, F.; Martínez, E., Surface properties and catalytic performance for ethane combustion of $La_{1-x}K_xMnO_{3+\delta}$ perovskites. *Appl. Catal. A-Gen.* **2001,** *207*, (1–2), 17–24.

(33) Fino, D.; Russo, N.; Saracco, G.; Specchia, V., The role of suprafacial oxygen in some perovskites for the catalytic combustion of soot. *J. Catal.* **2003,** *217*, (2), 367–375.

(34) Ma, L.; Wang, D.; Li, J.; Bai, B.; Fu, L.; Li, Y., Ag/CeO_2 nanospheres: efficient catalysts for formaldehyde oxidation. *Appl. Catal. B-Environ.* **2014,** *148*, 36–43.

(35) Bai, B.; Qiao, Q.; Arandiyan, H.; Li, J.; Hao, J., Three-dimensional ordered mesoporous MnO_2-supported Ag nanoparticles for catalytic removal of formaldehyde. *Environ. Sci. Technol.* **2016,** *50*, (5), 2635–2640.

(36) Kwon, D. W.; Seo, P. W.; Kim, G. J.; Hong, S. C., Characteristics of the HCHO oxidation reaction over Pt/TiO_2 catalysts at room temperature: the effect of relative humidity on catalytic activity. *Appl. Catal. B-Environ.* **2015,** *163*, 436–443.

(37) Zhang, C.; Li, Y.; Wang, Y.; He, H., Sodium-promoted Pd/TiO_2 for catalytic oxidation of formaldehyde at ambient temperature. *Environ. Sci. Technol.* **2014,** *48*, (10), 5816–5822.

(38) Wang, Y.; Zhu, X.; Crocker, M.; Chen, B.; Shi, C., A comparative study of the catalytic oxidation of HCHO and CO over $Mn_{0.75}Co_{2.25}O_4$ catalyst: The effect of moisture. *Appl. Catal. B-Environ.* **2014,** *160*, 542–551.

(39) Debono, O.; Thevenet, F.; Gravejat, P.; Hequet, V.; Raillard, C.; Lecoq, L.; Locoge, N.,

Toluene photocatalytic oxidation at ppbv levels: Kinetic investigation and carbon balance determination. *Appl. Catal. B-Environ.* **2016,** *106*, (3), 600–608.

(40) Weng, X.; Sun, P.; Long, Y.; Meng, Q.; Wu, Z., Catalytic oxidation of chlorobenzene over $Mn_xCe_{1-x}O_2$/HZSM-5 catalysts: a study with practical implications. *Environ. Sci. Technol.* **2017,** *51*, (14), 8057–8066.

(41) Li, H.; Cui, L.; Lu, Y.; Huang, Y.; Cao, J.-j.; Park, D.; Lee, S. C.; Ho, W. K., In situ intermediates determination and cytotoxicological assessment in catalytic oxidation of formaldehyde: implications for catalyst design and selectivity enhancement under ambient conditions. *Environ. Sci. Technol.* **2019,** *53*, (9), 5230–5240.

(42) Van de Vyver, S.; Odermatt, C.; Romero, K.; Prasomsri, T.; Román-Leshkov, Y., Solid Lewis acids catalyze the carbon-carbon coupling between carbohydrates and formaldehyde. *ACS Catal.* **2015,** *5*, (2), 972–977.

(43) Albonetti, S.; Blasioli, S.; Bonelli, R.; Mengou, J. E.; Scirè, S.; Trifirò, F., The role of acidity in the decomposition of 1,2-dichlorobenzene over TiO_2-based V_2O_5/WO_3 catalysts. *Appl. Catal. A-Gen.* **2008,** *341*, (1–2), 18–25.

(44) Selvakumar, S.; Nuns, N.; Trentesaux, M.; Batra, V.; Giraudon, J.-M.; Lamonier, J.-F., Reaction of formaldehyde over birnessite catalyst: a combined XPS and ToF–SIMS study. *Appl. Catal. B-Environ.* **2018,** *223*, 192–200.

(45) Islas, L.; Ruiz, J.-C.; Muñoz-Muñoz, F.; Isoshima, T.; Burillo, G., Surface characterization of poly (vinyl chloride) urinary catheters functionalized with acrylic acid and poly (ethylene glycol) methacrylate using gamma-radiation. *Appl. Surf. Sci.* **2016,** *384*, 135–142.

(46) Jia, X.; Ma, J.; Xia, F.; Xu, Y.; Gao, J.; Xu, J., Carboxylic acid-modified metal oxide catalyst for selectivity-tunable aerobic ammoxidation. *Nat. Commun.* **2018,** *9*, (1), 933–939.

(47) Chen, H.; Tang, M.; Rui, Z.; Wang, X.; Ji, H., ZnO modified TiO_2 nanotube array supported Pt catalyst for HCHO removal under mild conditions. *Catal. Today* **2016,** *264*, 23–30.

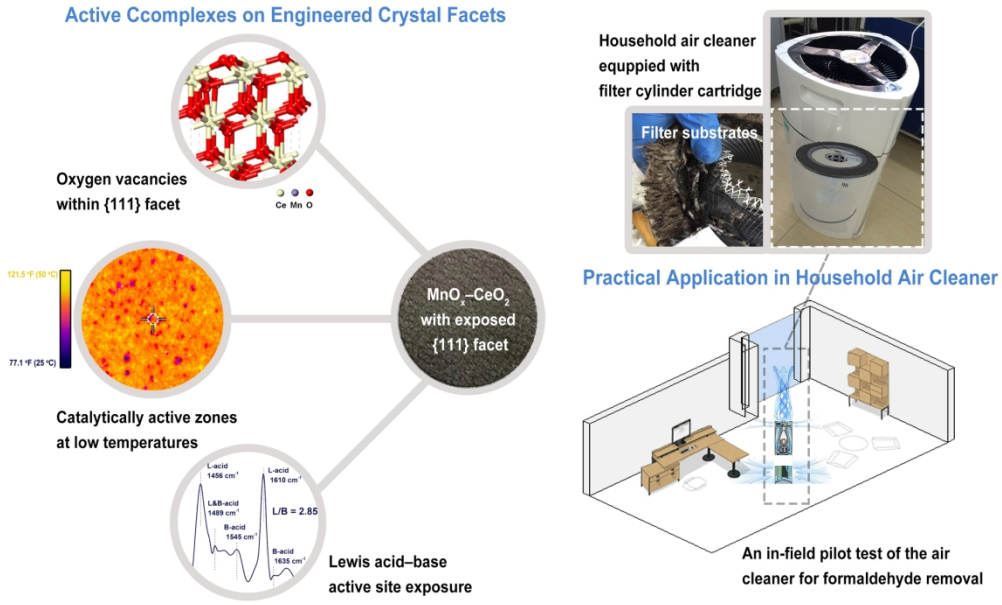

84x50mm (600 x 600 DPI)